

PAPER • OPEN ACCESS

Spontaneous topological charging of tactoids in a living nematic

Recent citations

- [Topological defects in active liquid crystals](#)
I S Aranson

To cite this article: Mikhail M Genkin *et al* 2018 *New J. Phys.* **20** 043027

View the [article online](#) for updates and enhancements.



PAPER

Spontaneous topological charging of tactoids in a living nematic

Mikhail M Genkin^{1,2} , Andrey Sokolov² and Igor S Aranson^{1,2,3}¹ Department of Engineering Sciences and Applied Mathematics, Northwestern University, 2145 Sheridan Road, Evanston, IL 60202, United States of America² Materials Science Division, Argonne National Laboratory, Argonne, IL 60439, United States of America³ Department of Biomedical Engineering, Pennsylvania State University, University Park, PA 16801, United States of AmericaE-mail: isa12@psu.edu**Keywords:** active nematic, living liquid crystal, tactoids, topological charge, motile bacteriaSupplementary material for this article is available [online](#)RECEIVED
29 November 2017REVISED
2 February 2018ACCEPTED FOR PUBLICATION
22 February 2018PUBLISHED
13 April 2018

Original content from this work may be used under the terms of the [Creative Commons Attribution 3.0 licence](#).

Any further distribution of this work must maintain attribution to the author(s) and the title of the work, journal citation and DOI.

**Abstract**

Living nematic is a realization of an active matter combining a nematic liquid crystal with swimming bacteria. The material exhibits a remarkable tendency towards spatio-temporal self-organization manifested in formation of dynamic textures of self-propelled half-integer topological defects (disclinations). Here we report on the study of such living nematic near normal inclusions, or tactoids, naturally realized in liquid crystals close to the isotropic-nematic (I–N) phase transition. On the basis of the computational analysis, we have established that tactoid's I–N interface spontaneously acquire negative topological charge which is proportional to the tactoid's size and depends on the concentration of bacteria. The observed negative charging is attributed to the drastic difference in the mobilities of $+1/2$ and $-1/2$ topological defects in active systems. The effect is described in the framework of a kinetic theory for point-like weakly-interacting defects with different mobilities. Our dedicated experiment fully confirmed the theoretical prediction. The results hint into new strategies for control of active matter.

1. Introduction

A class of non-equilibrium systems consisting of interacting agents transducing the energy stored in the environment into mechanical motion is often called active matter [1]. Examples range from bird flocks [2], fish schools [3], bacteria suspensions [4, 5], microtubules–molecular motors assays [6–8] to colloidal rollers [9] and Janus floaters [10]. Active systems often exhibit properties not present at their dynamic counterparts, such as viscosity reduction [11, 12], enhanced mixing [13, 14], rectification of chaotic motion [15, 16], active concentration depletion [17, 18] and many others.

An important class of active matter termed active nematic is constituted by active agents with apolar (nematic) interactions. A variety of systems fall into this class, from the suspension of swimming bacteria in nematic liquid crystal [19–21], gliding assays of microtubules or actin filaments on a lawn of molecular motors [22, 23], migrating cells in the cell tissues [24–26]. The recent studies demonstrated an extraordinary role of the topological defects ($\pm 1/2$ disclinations) in the spatio-temporal organization of these systems [21, 25, 26].

Up to date, most of the experimental and theoretical studies of active systems have focused on spatially-homogeneous systems where the role of the boundaries is not crucial. While active matter often coexists with an isotropic fluid, the proximity effects of isotropic fluid on active nematic are not well understood. Recent computational works [27, 28] studied the behavior of active nematic-isotropic mixtures. Active forces lead to undulation instability of the nematic/isotropic domains and ejection of $+1/2$ point topological defects in the bulk of the nematic phase. Consequently, the nematic-isotropic interface becomes negatively charged.

Macroscopic inclusions (tactoids) spontaneously appear in liquid crystal as a result of isotropic/nematic (I–N) phase transition controlled by temperature and the concentration of mesogenic material. Although the phase coexistence occurs in a narrow temperature interval, it can be expanded by the addition of surfactants [29].

It was experimentally observed, that bacteria in nematic phase swim around isotropic tactoids [19] and can be jammed in the tactoid's cusps [30].

Tactoids themselves play a profound role in many systems undergoing a phase transition. Besides liquid crystals, the examples include cosmological models of the early universe [31, 32], superfluidity [33, 34], solid state physics [35]. According to the Kibble–Zurek hypothesis of the early universe formation, after the symmetry-breaking phase transition, the domains with almost constant order parameter (OP) are created. Consequently, the domains with different OP orientation merge yielding topological defects. The shape and nematic structure of tactoids were the main focus of experimental and theoretical studies [36–40]. In these works, it is assumed that tactoid's size is determined by the interplay of elastic forces, surface energy and anisotropic anchoring on the I–N interface. In this context, the energy minimization problem has to be solved to find an optimum tactoid's shape. However, the role of tactoids on the properties of active nematics is not understood.

Here we perform computational and experimental studies on the role of tactoids in the organization of active collective motion. Tactoids are explicitly incorporated in an extended model of a living nematic [21]. The obtained nematic configurations are in good agreement with the experiments [36, 37]. We have found that in the regime of active turbulence the tactoid's isotropic-nematic interface spontaneously acquires an average negative topological charge. These findings are rationalized in the framework of a simple kinetic model for two populations of point-like weakly-interacting defects with different mobilities. The dependence of a tactoid's charge on the bacteria concentration and tactoid's size is in a good agreement with computations. To support our theoretical predictions, we performed a dedicated experiment with swimming bacteria *Bacillus subtilis* suspended in a lyotropic chromonic disodium cromoglycate (DSCG) liquid crystal. Our experimental results agrees with computational modeling both qualitatively and quantitatively.

2. Description of computational model

2.1. Model

The model is a significant extension of our previous study [21]. A continuum approach is justified by the fact that characteristic length scale of the emergent patterns (for example, an average distance between topological defects) $L \sim 200 \mu\text{m}$ significantly exceeds average inter-bacterial distance $l < 10 \mu\text{m}$. For the liquid crystal dynamics we use continuum 2D (depth-averaged) Edwards–Beris approach:

$$(\partial_t + \vec{v} \cdot \nabla) \mathbf{Q} - \mathbf{S} - \Gamma \mathbf{H} + \mathbf{F}_{\text{exter}} + \mathbf{F}_{\text{anch}} = 0, \quad (1)$$

$$\nabla \cdot (\boldsymbol{\sigma}_a + \boldsymbol{\sigma}_s + \boldsymbol{\sigma}_{\text{act}} + \boldsymbol{\sigma}_{\text{visc}} - p \mathbf{I}) - \zeta \vec{v} = 0, \quad (2)$$

$$\nabla \cdot \vec{v} = 0. \quad (3)$$

Here equation (1) describes the tensorial order parameter (OP) \mathbf{Q} evolution, which is defined as $\mathbf{Q} = q(\vec{n}\vec{n} - \mathbf{I}/2)$, where \vec{n} is the unit vector of nematic orientation, q is the amplitude of the OP. Tensor \mathbf{S} describes alignment with the fluid flow, \mathbf{H} is the tensorial molecular field and $\mathbf{F}_{\text{exter}}$ is the external (wall) anchoring. Tensor \mathbf{F}_{anch} is a new term that describes anisotropic anchoring on the I–N interface. Equation (2) is the linear momentum balance, where we split the total stress tensor into isotropic $\boldsymbol{\sigma}_s$, anisotropic $\boldsymbol{\sigma}_a$, viscous $\boldsymbol{\sigma}_{\text{visc}}$ and active $\boldsymbol{\sigma}_{\text{act}}$ contributions. The last term in equation (2) is the contribution from the depth-averaging. Equation (3) is the incompressibility condition. For the detailed definitions of the mentioned terms see appendix A.

We couple equations (1)–(3) with the conservation laws for the bacteria concentration c that are cast in the form of advection-diffusion equations:

$$\begin{aligned} \partial_t c + \nabla \cdot (V_0 \vec{p} w + \vec{v} c) &= D_c \nabla^2 c, \\ \partial_t w + \nabla \cdot (V_0 \vec{p} c + \vec{v} w) &= -\frac{2w}{\tau} + D_c \nabla^2 w. \end{aligned} \quad (4)$$

As in our previous work [21], we assume that at each point we have two concentrations of bacteria c^+ and c^- swimming with a constant speed V_0 along the directions \vec{p} and $-\vec{p}$ correspondingly. Here $\vec{p} = (\cos(\phi), \sin(\phi))$, where ϕ is the local orientation angle of bacteria. Equation (4) describes evolution of the total concentration field $c = c^+ + c^-$ and the concentration difference (or polarization) field $w = c^+ - c^-$. Here we allow bacteria reversal with the average rate τ . For additional details see [21].

The major difference with [21] is that the bacteria swimming direction \vec{p} does not coincide with the nematic (director) orientation vector \vec{n} . This generalization is needed because the nematic director \vec{n} is not defined in the isotropic phase. According to [21], angle ϕ obeys the following relaxation equation

$$\partial_t \phi = \frac{|\mathbf{Q}|}{\tau_0} \sin(2\theta - 2\phi) + D_t \nabla^2 \phi. \quad (5)$$

Here the first term describes the relaxation towards the nematic angle θ with the relaxation rate τ_0 , and the second term describes the diffusion of orientation with the rate D_t . The rationale for the choice of $\sin(2\theta - 2\phi)$ term in equation (5) is the following. Since $\theta - \phi$ is a periodic function, the angle relaxation has to be governed by a periodic function as well, e.g. by a sine: a leading term in the expansion of a generic periodic function. Note that the relaxation towards the nematic director (due to elastic restoring torque) is taken to be proportional to the angle difference $\theta - \phi$, see [41, 42]. This torque also has to satisfy several limiting conditions, e.g. at $\theta - \phi = \pi/2$ it has to vanish. In equation (5) we used a different form (sine of the angle difference) that automatically satisfies the required limiting conditions. We observed that for typical relaxation time $\tau_0 \approx 1$ s, the bacterial orientation always coincides with the director in the nematic phase, which makes the difference $\theta - \phi$ very small. Since $\sin x \approx x$ for small x , our approach is equivalent to the conventional one [42].

In normal domains, where $|\mathbf{Q}| = 0$, the alignment term $|\mathbf{Q}|\sin(2\theta - 2\phi)$ disappears and bacterial orientation is governed purely by the diffusion term. For simplicity, we assume that the elastic effects in LC dominate the flow alignment and neglect the advection and shear alignment terms (these terms will not change our results qualitatively, provided that the relaxation time τ_0 is sufficiently small). Equation (5) is difficult to solve numerically due to angle discontinuity. Here, by analogy with the nematic tensor \mathbf{Q} , we introduce an evolution equation for the traceless symmetric tensor $\mathbf{P} = q_p(\vec{p}\vec{p} - \mathbf{I}/2)$ for bacterial orientation:

$$\partial_t \mathbf{P} = a_p \mathbf{P} - 4c_p \mathbf{P}^3 - \frac{\mathbf{F}_Q}{\tau_0} + D_t \nabla^2 \mathbf{P}. \quad (6)$$

Here a_p and c_p are constants that control the amplitude $q_p = |\mathbf{P}|$ and that are chosen in such way that $q_p = 1$ in the steady-state. \mathbf{F}_Q aligns \mathbf{P} with the nematic orientation set by tensor \mathbf{Q} with the alignment time τ_0 (τ_0 is of the order 1 s and is much smaller than the bacteria reversal time $\tau \approx 60$ s [21]). The alignment term $\mathbf{F}_Q \sim \mathbf{Q}$ is chosen in such way that it does not change the amplitude of tensor \mathbf{P} . In the limit $|\mathbf{P}| = \text{const}$ we recover equation (5). For the definition of \mathbf{F}_Q see appendix A. Inside the tactoid, \mathbf{F}_Q vanishes, and bacterial orientation becomes independent of \mathbf{Q} . In turn, the nematic tensor \mathbf{Q} couples to the tensor \mathbf{P} via the expression for active stress. Note, that the constants a_p and c_p are used to control the amplitude q_p of the tensor \mathbf{P} and do not bear any physical meaning (unlike similar terms a and c in the equation for the OP \mathbf{Q}).

Our model consists of equations (1)–(4), (6). The major differences of this study from our previous work [21] include: (i) introduction of an additional equation for the bacterial orientation (6), (ii) introduction of the isotropic phase in the form of a tactoid (see section 2.2) and (iii) anisotropic anchoring on the I–N interface. Note, that the anchoring on the I–N interface is typically described by the Rapini–Papoular form [43]. We implemented the I–N anchoring in a different way by introducing additional relaxation term \mathbf{F}_{anch} in equation (1). It can be shown that our approach is equivalent to Rapini–Papoular one, see appendix D.

2.2. Tactoid implementation

In the biphasic domain, the tactoids can be introduced in the Landau–de Gennes free energy via additional term $\sim |\mathbf{Q}|^4$. This term will make both isotropic and nematic states locally stable. However, since we are interested in fixed isotropic domains (they can be produced, for example, by local heating), we make the coefficient a in front of the quadratic term in the Landau–de Gennes free energy (see appendix A for the definition of free energy) spatially-dependent, so that the equilibrium OP's amplitude q is some positive constant in nematic and zero in isotropic phase, see figure 1 where amplitude $q = |\mathbf{Q}|$ is shown with color.

Consider a nematic phase and suppose we want to introduce an isotropic tactoid. In order to do that, we set the coefficient a to a negative value inside the tactoid, $a = -a_2$, and positive value outside of the tactoid, $a = a_1$ with a rapid, but continuous transition on the I–N boundary. To implement a tactoid defined by the equation $f(x, y) \leq 0$, with boundary $f(x, y) = 0$, we set:

$$a(x, y) = -\frac{a_1 + a_2}{2} \left(\tanh\left(-\frac{f(x, y)}{\delta}\right) + 1 \right) + a_1. \quad (7)$$

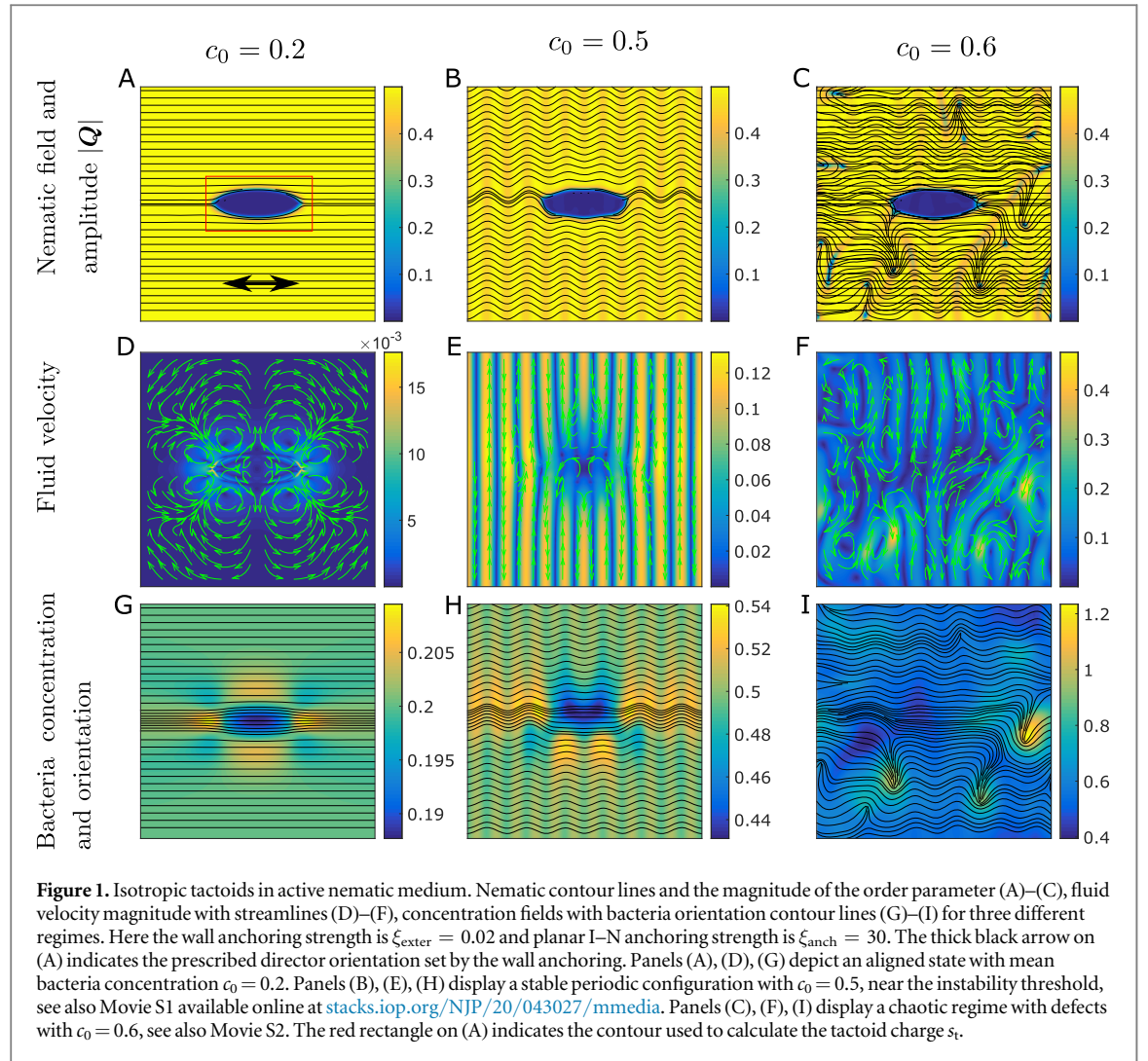
Here δ is an approximate width of the I–N interface (the actual width of the I–N interface also depends on the other parameters). In this work we used $a_1 = 1$, $a_2 = 5$. We considered isotropic tactoids of elliptical shape:

$$f_I(x, y) = \frac{(x - x_0)^2}{R_1^2} + \frac{(y - y_0)^2}{R_2^2} - 1. \quad (8)$$

In order to create a nematic tactoid surrounded by an isotropic phase, we changed the sign of the coefficient a to an opposite one in the entire computational domain. We considered nematic tactoids of circular shape:

$$f_N(x, y) = \frac{(x - x_0)^2}{R_0^2} + \frac{(y - y_0)^2}{R_0^2} - 1. \quad (9)$$

Thus, we introduced tactoids in our system by spatial variation of the Landau–de Gennes coefficient a . In our simplified approach, the tactoid shape is predefined (although local shape adjustments can take place near the



surface defects, or boojums, see figure 3(C). Although more complicated models [27] of the biphasic systems with the possibility of shape evolution can be considered, our experimental observations justify our assumption of nearly fixed tactoid's shape (see Movie 4).

2.3. Numerical implementation

Nonlinear system of PDEs (1)–(4), (6) was integrated in a square domain with periodic boundary conditions, 1024×1024 mesh points were typically used. Other numbers of mesh points were also used to ensure that the chosen resolution is an optimal one and to exclude numerical artifacts. We used a combination of forward Euler method in time and pseudospectral method in space for the numerical integration, see appendix A. Initial conditions were either aligned along the x -axis with small noise or random from uniform distribution.

2.4. Additional implementation details

There was an artifact related to the definition of the bacteria orientation angle ϕ that was restricted to the interval $\phi \in [-\pi/2; \pi/2]$. We solved this problem by relabeling the concentrations c^+ and c^- in the close proximity of the regions where $\phi = \pm\pi/2$. For additional implementation details see [21] (where the same thing was performed for the nematic angle θ).

In addition, there was a discrepancy related to the fact, that nematic field is not defined in the defect core. We modified our scheme by significantly reducing the reversal time τ (see equation (4)) in the close proximity of each defect core. This was performed by scaling τ by the factor $|p|^6$ in the entire computational domain. This factor was approximately 1 nearly everywhere (including both nematic and isotropic phases), but in the cores of topological defects where it was very small. By using this technique, we significantly reduced the concentration difference w in the cores of topological defects, which is equivalent to setting $c^+ \approx c^-$ (there is no difference between c^+ and c^- at the singularity point).

2.5. Experimental details

The procedure of the living nematic sample preparation and data acquisition is similar to methods used in previous works [19, 21]. We used nearly crossed polarized microscopy for simultaneous visualization of bacteria and tactoids. The data was recorded with frame rate of 15 fps using $10\times$ magnification. Bacterial concentration in the experiment was $c_0 \approx 5 \times 10^9$ cells cm^{-3} .

The experiment was performed in a flat glass/PDMS cell. A small ($\approx 10 \mu\text{l}$) drop of bacterial suspension in DSCG was sandwiched between a TiO_2 coated glass slide and a polydimethylsiloxane (PDMS) film. $20 \mu\text{m}$ spacers were used to ensure uniform thickness over the cell. The thickness of the PDMS film was chosen to be approximately 1 mm, as a trade-off between the film stiffness and the oxygen permeability. In order to keep the system in the biphasic state, a small electric current was transmitted through a TiO_2 coated glass slide to heat the LC and create isotropic tactoids of various sizes. The temperature of the sample was in the range of $T \approx 25^\circ\text{C} - 30^\circ\text{C}$.

The nematic field was reconstructed with a custom Matlab script. The orientation of each bacterium and correspondingly nematic field in its vicinity was extracted from grayscale images by a gradient method. Assuming that an orientation of LC molecules changes slowly between the neighboring bacteria, we reconstruct the nematic field by linear interpolation. The field was smoothed out by a Gaussian low-pass filter with a standard deviation equals to the average bacterial length of $5 \mu\text{m}$. To increase the accuracy of the method in areas where bacteria swim occasionally, we time-averaged the field over 50 consecutive frames.

3. Results

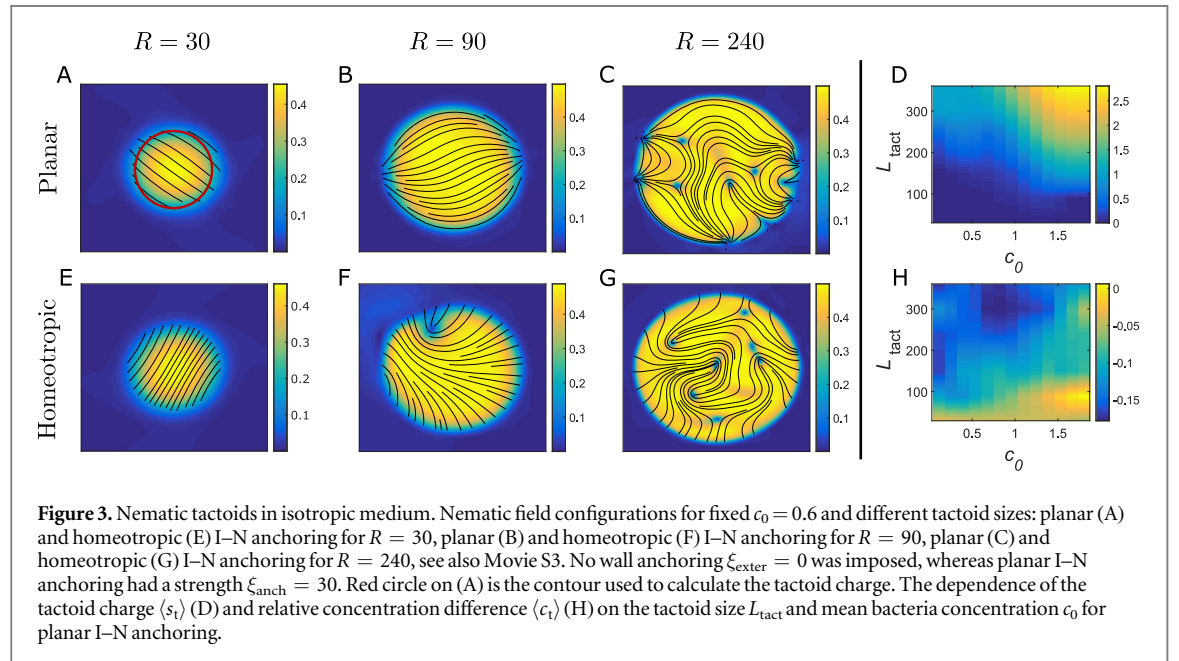
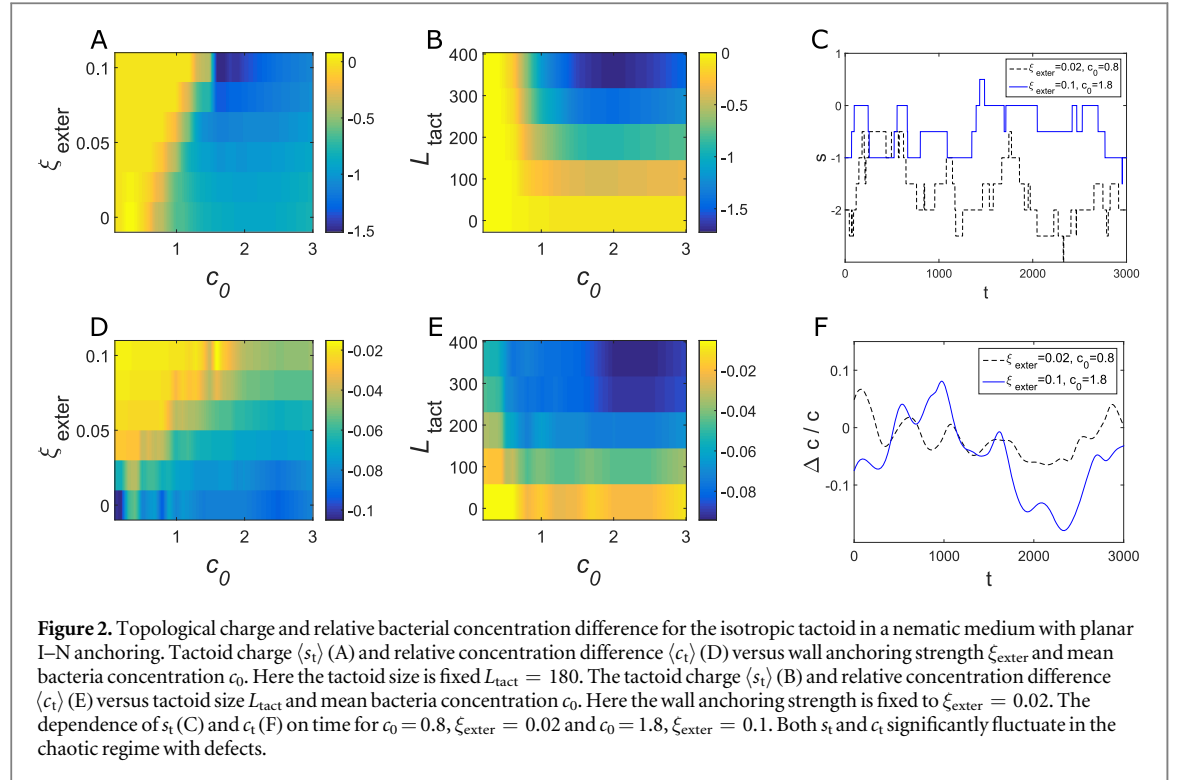
3.1. Isotropic tactoids in nematic phase

Isotropic tactoids in nematic phase with planar I–N anchoring are shown in figure 1. At sufficiently low bacterial concentrations and high wall anchoring (wall anchoring prescribes the overall nematic orientation, see appendix A and [21]), an aligned regime with the nematic orientation parallel to the anchoring direction was observed, figure 1(A). However, planar I–N anchoring forces the nematic orientation to deviate from the horizontal one in the tactoid proximity. The velocity for this case is very small, and attains the maximum value on the I–N interface near the tactoid's cusps (due to non-zero gradients of the OP), figure 1(D). In this case, the bacteria concentrate outside of the tactoid near the cusps, whereas bacteria concentration is reduced inside the tactoid, figure 1(G). For moderate bacteria concentrations, the configuration is characterized by periodic nematic undulations, figure 1(B). In this case, the hydrodynamic flow forms lanes normal to the anchoring direction, figure 1(E). As in the previous case, the bacteria concentrate outside of the tactoid. However, the interplay of wall anchoring at the I–N interface and the bulk nematic orientation results in non-symmetric flow structure around a tactoid, figure 1(H). For even higher bacteria concentrations, a chaotic regime with multiple topological defects was observed, figures 1(C), (F), (I). The defects enter and leave the tactoid and temporarily distort the planar anchoring at the I–N interface.

Note that the instability threshold observed here and in our previous work is different from the isotropic case, where the system is always appears to be unstable [44]. This is because of an additional alignment introduced by the nematic field. By comparing the perturbation torque generated by active stress, which is proportional to the bacterial concentration $T_{\text{act}} = k_1 c \phi$ with the restoring elastic (or external wall anchoring) torque $T_{\text{elastic}} = k_2 \phi$, one can justify that the former exceeds the latter only for $c > k_2/k_1$.

We measured time-averaged total topological charge of the tactoid s_t and averaged relative bacteria concentration inside the tactoid c_t : $c_t = \langle (c_{\text{tact}} - c_0)/c_0 \rangle$, c_{tact} is the space-averaged concentration inside the tactoid, c_0 is mean bacteria concentration, $\langle \rangle$ denotes time-averaging. The charge was calculated from the phase difference in the counterclockwise direction over a region enclosing the tactoid (red rectangle in figure 1(A)), see appendix A.

The dependences of topological charge s_t and concentration c_t on wall anchoring and bacteria concentration c are shown in figures 2(A), (D) (planar I–N anchoring). For small bacteria concentrations and strong wall anchoring, there are no topological defects and the tactoid's topological charge is zero. For higher concentrations, in the regimes with defects, the average topological charge of the tactoid is always negative. The charge magnitude first increases with the bacteria concentration but then saturates and falls down. The magnitude of the tactoid's charge increases with the wall anchoring. There is also a minor suppression of the relative bacteria concentration inside the tactoid. The dependences of s_t and c_t versus tactoid's size and mean bacteria concentration are shown in figures 2(B), (E). In this work, we fixed the aspect ratio of isotropic tactoids at 1:3 and defined tactoid's size as the length of its major axis. Both magnitudes of s_t and c_t grow linearly with the tactoid size. Similar behaviors are also observed for the tactoids with homeotropic I–N anchoring, see appendix B. Note, that as long as the defects are persistently entering and leaving the tactoid, instant topological charge \tilde{s}_t and relative bacteria concentration \tilde{c}_t significantly fluctuate with time, see figures 2(C), (F).



3.2. Nematic tactoids in isotropic phase

Nematic tactoids in isotropic phase can be produced by changing the sign of the Landau–de Gennes coefficient a in the entire computational domain. In agreement with experiments [36], we obtained different nematic configurations versus bacteria concentrations and tactoid sizes. We studied the tactoids of circular shape with different radii R , and no wall anchoring. Configurations with mean bacteria concentration $c_0 = 0.6$ for planar I-N anchoring and different tactoid sizes are shown in figures 3(A)–(C) and for homeotropic I-N anchoring are shown in figures 3(E)–(G). The obtained configurations are in good qualitative agreement with the experiment: for small tactoid size, the elastic forces dominate over surface anchoring, which corresponds to aligned (undisturbed) nematic configuration (figures 3(A), (E)). For larger tactoid sizes, there were a few singularities on the tactoid's surface (figures 3(B), (F)). For even larger tactoid sizes, configurations with many defects are observed, both inside the tactoid and on its surface. The singularities on the I-N interface are called boojums. Figure 3(B) depicts the so-called '2c' configuration with 2 positive boojums that frequently arises in experiments

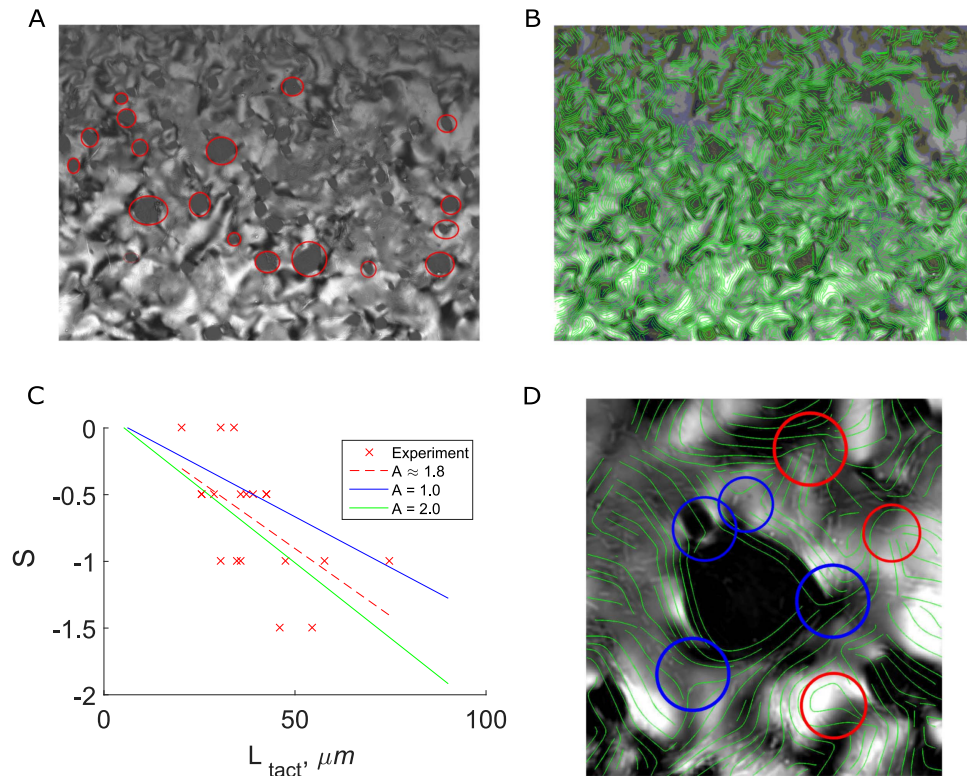


Figure 4. Experimental images of isotropic tactoids in nematic medium and comparison of the data from experiments and simulations. (A) An experimental image obtained by nearly-cross polarized microscopy. 17 visible tactoids are encircled, see also Movie S4. (B) Nematic field (green lines) reconstructed from orientation of bacteria in 50 consecutive frames. (C) The dependence of tactoid's topological charge on its size obtained from the experiment (crosses) and simulations (solid lines). Activity of bacteria A , a product of bacterial concentration c_0 and dipole force strength, is extracted from linear fit (dashed line) of the experimental data. The bacterial concentration in the experiment was 5×10^9 cells cm^{-3} . (D) Nematic configuration around a single tactoid in the experiments. Positive defects are highlighted with red circles, negative with blue circles. Negative defects reside on the I-N interface, whereas positive ones in the bulk of nematic phase.

(see e.g. [36, 38]). Note that even though the overall tactoid shape was predefined (disk), there was a local shape adjustment near the boojums, figure 3(C), (F).

We measured averaged charge s_t and relative bacteria concentration inside the tactoid c_t . To determine the tactoid charge, we calculated the phase difference over a circular contour with $R = 0.99 R_0$, R_0 is the radius of the tactoid (red circle in figure 3(A)). Thus, we calculated the total topological bulk charge and did not take into account the charge produced by boojums on the I-N interface. Both s_t and c_t versus tactoid size and mean bacteria concentration are shown in figures 3(D), (H) for planar I-N anchoring (dependencies for homeotropic anchoring are shown in appendix B). For both planar and homeotropic anchorings, the averaged bulk tactoid's charge is positive and grows with the bacteria concentration and tactoid's size. Note, that due to topological charge conservation, it implies negative surface topological charge, so that I-N interface becomes negatively charged as in the case of isotropic tactoid, see section 3.1. The relative concentration difference inside the tactoid is always negative for planar anchoring, with its maximum (by absolute value) achieved for large tactoids and intermediate bacteria concentrations. For high bacterial concentrations, in highly chaotic regimes, the effect smears out. For the homeotropic case, relative concentration difference is positive, see appendix B.

3.3. Experimental verification

Experimental verification was performed with strain 1085 of motile bacteria *Bacillus subtilis* suspended in lyotropic liquid crystal DSCG, see section 2.4. The microscopy images were acquired in nearly cross-polarized regime, where the angle between a polarizer and an analyzer was slightly less than $\pi/2$, figure 4(A). This regime allows to observe both swimming bacteria and tactoids seen as dark areas simultaneously. Images were processed with a custom Matlab script to reconstruct the nematic field from the local orientation of bacteria, figure 4(B). Topological charges of 17 visible tactoids were determined by summing the topological charges of defects around each of tactoids, figure 4(D). The analysis of the experimental data reveals that the total topological charge is decreasing with the size of a tactoid, confirming theoretical predictions, see figure 4(C).

The accessible range of bacterial concentration in the experiments is limited by two factors. At low concentrations, the nematic field can not be reconstructed in significantly large areas due to the absence of

bacterial tracers. At high concentrations tracking of bacterial orientation is not reliable due to bacterial overlapping. These limitations may be overcome by adding passive fluorescent orientational tracers into the system in future work.

4. Discussion

The onset of tactoid spontaneous charge can be attributed to different defect mobilities in active systems: $+1/2$ are mobile, whereas $-1/2$ are effectively immobile and only entrained by the moving ones [25, 45, 46]. In [21], we have found that the effective speed of $+1/2$ defects is approximately 5 times larger than of $-1/2$ defects. In order to enter or leave the tactoid, the defects need to overcome a barrier at the I–N interface. We verified that the barrier is practically independent of the anchoring strength and is due to sharp variation of the nematic OP across the interface. The barrier breaks the symmetry in $\pm 1/2$ defect absorption and leads to a non-uniform defect distribution, and thus net charging. The charging increases with the bacteria concentration, since the defect concentration itself is proportional to the bacteria concentration [21]. However, at very large bacteria concentrations, the charging is overwhelmed by the inter-defect interactions.

To support our hypothesis, we developed a stationary 1D Fokker–Plank description for positive and negative defects probability distribution functions P^+ and P^- , see also appendix C and figure C1. We took into account different defects mobilities (manifested by different diffusion coefficients) and pairwise interactions between the defects: this interaction is similar to the Coulomb interactions between charged particles (different signs attract, similar signs repel) but with the interaction force inversely proportional to the distance between defects $F \propto 1/r$ [47].

$$\begin{aligned} D^+ \partial_x^2 P^+ &= \partial_x \left(\mu \int_0^L \frac{P^+(x') - P^-(x')}{x - x'} dx' P^+ - F'(x) P^+ \right), \\ D^- \partial_x^2 P^- &= \partial_x \left(\mu \int_0^L \frac{P^-(x') - P^+(x')}{x - x'} dx' P^- - F'(x) P^- \right). \end{aligned} \quad (10)$$

Here D^\pm are the defect diffusivities, $D^+ \gg D^-$, μ is the inter-defect interaction strength, $F(x)$ describes a potential barrier at the I–N interface, and L is the total size of the system. Here we assume that the defect diffusivities are roughly proportional to the product of defect speed and its mean free path, which in turn depend on the concentration of bacteria. Note, that the description of defect's motion with diffusion-like process is justified by the fact that at sufficiently high bacterial concentration defect statistics can be well-approximated by the Gaussian distribution [21] (in contrast to the stretched exponent distribution that is typical for ballistic defects).

For equation (10), an asymptotic solution for the tactoid charge density can be obtained under the assumption of very large positive defect diffusivity D^+ and weak defects interaction (see appendix C):

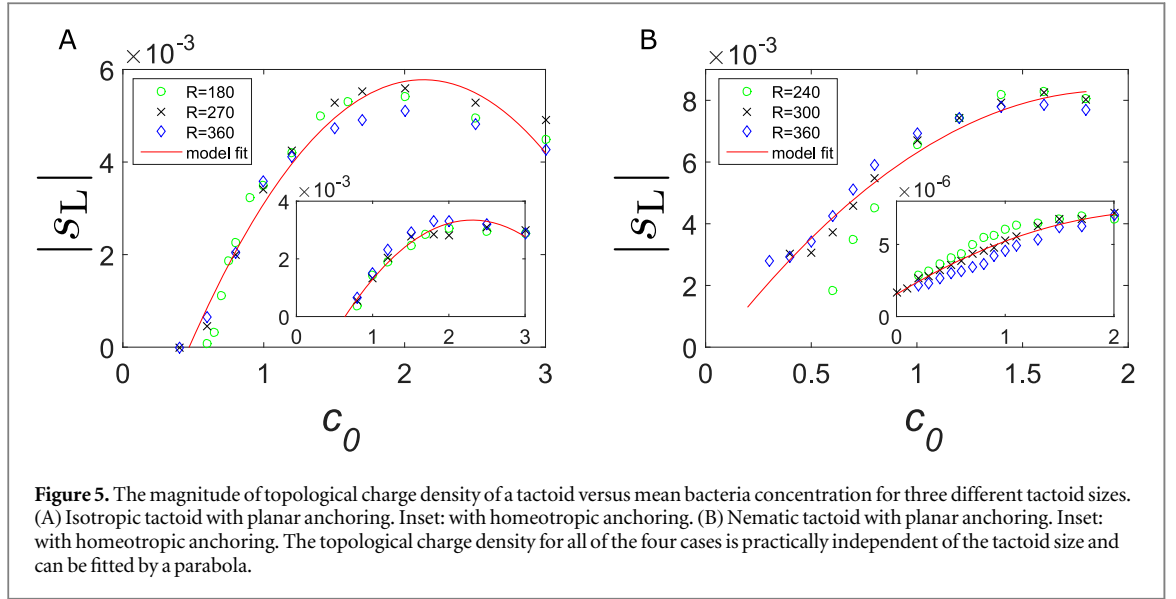
$$S = -P_0 \delta (e^{\frac{A}{D^-}} - 1) \left(1 - \frac{\mu \delta P_0 e^{\frac{A}{D^-}}}{D^-} \left(\log \frac{L}{\delta} + 1 \right) \right). \quad (11)$$

Here S is the tactoid topological charge density, P_0 is the mean defect density in the system (assumed to be proportional to the bacterial concentration c), δ is the width of I–N interface, A is the height of the potential barrier.

This model explains spontaneous negative charging of the I–N interface if we assume $A > 0$. It will immediately imply accumulation of negative charge for negative tactoids and vice versa. The charge magnitude depends on the mean defect (or bacteria) concentration as $S \propto -C_0 P_0 + C_1 P_0^2$ with $C_0 > C_1$, where $C_{1,2}$ are constants. Moreover, as long as we assumed that the defects exist only at the nematic medium or at the I–N interface, the charge density is independent of the tactoid's size. Charge density decreases with the system size as $S \propto -\log L/\delta$. The logarithmic divergence of S with the system size is an artifact of the assumption that the interaction strength between moving defects is $1/r$, similar to the immobile ones. As was shown, see e.g. [48], a small velocity correction to the interaction force leads to regularization of the logarithmic divergence.

The correspondence of the suggested simplified 1D and full 2D models becomes clear if one considers the case of the very strong external (wall) anchoring along the x -axis. In this case [21], all topological defects are moving predominantly along the direction normal to the wall anchoring (along the y -axis) so that the 2D system is equivalent to a quasi-1D system. In this one-dimensional representation, two defects, that are separated along the x -axis, can pass through each other without collision.

Topological charge density, defined as a ratio of the tactoid topological charge to its length $s_L = s_t/L$ for different tactoid sizes and bacterial concentrations are shown in figures 5(A), (B). This data is extracted from figures 2, 3 and appendix B. One sees that for isotropic and nematic tactoids with planar and homeotropic I–N anchoring, the tactoid topological charge density versus concentration is practically independent of the tactoid's



size and can be well approximated by a parabola, in agreement with equation (11). In addition, we calculated the tactoid charge for the isotropic rectangular tactoid that span along the entire horizontal direction (see appendix B) with a variable width h along the y -axis. We fixed the total system size, thus with h increasing the size of the medium L was decreasing. We found out, that tactoid topological charge is practically independent of L and h for sufficiently small bacteria concentrations. However, there is a steep increase in the topological charge for large L that is probably associated with a very small tactoid width h , so that topological defects are able to traverse the tactoid.

5. Conclusions

Here we investigated model of active nematic system in the biphasic regime. In our approach, the nematic and isotropic phases are created by spatial modulation of the Landau–de Gennes coefficient a . Even though the overall tactoid shape was predefined, local dynamical shape adjustments take place, e.g. near the negative boojums, figure 3(C). We implemented a nematic-dependent anisotropic anchoring and showed that our approach is equivalent to the conventional approach with additional contribution to the free energy in the Rapini–Papoular form, see appendix D. The main difference from our previous model [21] is an additional equation for the bacteria orientation required to prescribe bacterial motion inside the tactoid.

We have found that the tactoids spontaneously acquire a non-zero topological charge. The charge density depends on the mean bacterial concentration and wall anchoring strength. This effect is illustrated and quantified with a simple 1D Fokker–Plank model that attributes spontaneous charge accumulation to different defect mobility. The model qualitatively captures the dependence of the tactoid topological charge on the mean bacterial concentration, tactoid size, and the system size. Our experiment fully confirms the prediction and shows qualitatively and quantitatively similar dependence of the I–N charge for different tactoid sizes. The suggested mechanism is similar to that of spontaneous charging of colloids [49, 50] due to colloidal particles protonation and transport of mobile protons into the solution. Note that the tactoid charging is fundamentally different from topological defect pinning by material imperfections in equilibrium systems, e.g. pinning of vortices in type-II superconductors [51]. Whereas superconducting vortices are pinned by the imperfections irrespective of their sign, the topological defects show remarkable asymmetry in their pinning properties.

Our work provides a better insight into the complex interactions between the topological defects and tactoids in non-equilibrium systems. Both topological defects and tactoids can be used as tools to control and manipulate active matter. Topological defects can be created and controlled by light [52, 53] or by atomic force surface-patterning [54]. Correspondingly, tactoids can be created by intense laser heating and controlled by electric or magnetic fields. It was reported that tactoids can be reversibly aligned and stretched by up to a factor of fifteen in length using an electrical field [55]. Our findings suggest that an array of tactoids created on demand can be used to capture negative defects and thus create a positively charged active nematic liquid. This can potentially introduce additional control capabilities over active matter as well as a new way of sorting and identifying bacteria in addition to other methods [56].

Acknowledgments

MMG, AS and ISA were supported by the US Department of Energy, Office of Basic Energy Sciences, Division of Materials Science and Engineering (experimental work and simulations performed at ANL). ISA was also supported by the NSF grant PHY 1707900 (analysis of the Fokker–Plank system for the defects).

Author Contributions

ISA conceived the research. ISA and MMG developed the theory. MMG performed modeling and computing. And AS performed experiments and analyzed data. All authors wrote the manuscript.

Competing Interests

The authors declare that they have no competing financial interests.

Appendix A. Computational model

A.1. Definitions

Our nonlinear system consists of equations (1)–(4), (6). Both the OP and the bacterial orientation tensors are 2×2 traceless symmetric tensors that are defined as follows:

$$\mathbf{Q} = q(\vec{n}\vec{n} - \mathbf{I}/2), \quad \mathbf{P} = q_p(\vec{p}\vec{p} - \mathbf{I}/2). \quad (\text{A.1})$$

Here q and q_p are the amplitudes of the corresponding tensors, \vec{n} is nematic director, \vec{p} is bacteria orientation, \mathbf{I} is a 2×2 unit matrix. In equation (1) tensor \mathbf{S} can be expressed thorough the symmetric \mathbf{A} and antisymmetric Ω contributions of the velocity gradient tensor $\mathbf{W} = \nabla \vec{v}$:

$$\mathbf{S} = (\xi \mathbf{A} + \Omega) \left(\mathbf{Q} + \frac{\mathbf{I}}{2} \right) + \left(\mathbf{Q} + \frac{\mathbf{I}}{2} \right) (\xi \mathbf{A} + \Omega) - \xi (2\mathbf{Q} + \mathbf{I}) \text{Tr}(\mathbf{Q}\mathbf{W}), \quad (\text{A.2})$$

where ξ is an aspect ratio parameter. The molecular field \mathbf{H} can be defined as a first variation of Landau–de Gennes free energy F . Here we use one-constant elastic approximation:

$$F = \int d\vec{r} \left[-\frac{a}{2} Q_{\alpha\beta} Q_{\beta\alpha} + \frac{b}{4} (Q_{\alpha\beta} Q_{\beta\alpha})^2 + \frac{K}{2} (\partial_\gamma Q_{\alpha\beta})^2 \right], \quad (\text{A.3})$$

$$\mathbf{H} = a\mathbf{Q} - c\mathbf{Q} \text{Tr} \mathbf{Q}^2 + K \nabla^2 \mathbf{Q}. \quad (\text{A.4})$$

The external wall anchoring $\mathbf{F}_{\text{exter}}$ relaxes director towards a certain anchoring direction defined by unit vector \vec{f}_{ext} . The form of this term is chosen such as it does not affect the amplitude q , see also [21]:

$$\mathbf{F}_{\text{exter}} = 4\xi_{\text{exter}} \mathbf{Q} \mathbf{R}_{\pi/2} \text{Tr}[\mathbf{Q}(\vec{f}_{\text{ext}}\vec{f}_{\text{ext}} - \mathbf{I}/2) \mathbf{R}_{\pi/2}], \quad (\text{A.5})$$

where ξ_{exter} is the strength of external anchoring, $\mathbf{R}_{\pi/2}$ is the rotation matrix. In this work we always choose the external (wall) anchoring direction along the x -axis: $\vec{f}_{\text{ext}} = (0; 1)$.

The alignment of the LC director on the I–N interface is described by the term \mathbf{F}_{anch} :

$$\mathbf{F}_{\text{anch}} = 4\xi_{\text{anch}} \mathbf{Q} \mathbf{R}_{\pi/2} \text{Tr}[\mathbf{Q}(\vec{f}_e\vec{f}_e - \mathbf{I}/2) \mathbf{R}_{\pi/2}] \mathcal{I}(\vec{r}). \quad (\text{A.6})$$

Here ξ_{anch} is the strength of I–N anchoring, \vec{f}_e is a vector along the easy direction on the I–N interface (see [36]), $\mathcal{I}(\vec{r})$ is a step function that is non-zero only in a thin region that encloses I–N interface. The form of the term \mathbf{F}_{anch} is similar to the form of other relaxation terms, for example, $\mathbf{F}_{\text{exter}}$.

In order to find \vec{f}_e , we rotated the normal vector to the I–N interface (which we set parallel to the OP's amplitude gradient) by the easy angle:

$$\mathbf{f} = \mathbf{R}_{\theta_0}(\nabla|\mathbf{Q}|). \quad (\text{A.7})$$

Here \mathbf{R}_{θ_0} is the rotation matrix by the easy angle θ_0 . In this work, we only considered planar ($\theta_0 = \pi/2$) and homeotropic ($\theta_0 = 0$) anchoring. Note, that we did not normalize easy direction vector, therefore the normalization factor $|\vec{\nabla}|\mathbf{Q}||^2$ will be absorbed in the amplitude ξ_{anch} (see equation (D.10)).

Different stress contributions $\sigma_s, \sigma_a, \sigma_{\text{act}}, \sigma_{\text{visc}}$ in equation (2) are the same as in our previous work, see [21].

Equation (6) contains the term \mathbf{F}_Q that represents a relaxation of the bacterial orientation tensor \mathbf{P} towards the nematic orientation \mathbf{Q} . The form of this term is similar to the other relaxation terms:

$$\mathbf{F}_Q = \frac{4}{\tau_0} \mathbf{P} \mathbf{R}_{\pi/2} \text{Tr}(\mathbf{P} \mathbf{Q} \mathbf{R}_{\pi/2}). \quad (\text{A.8})$$

This term relaxes bacteria orientation defined by the tensor \mathbf{P} towards the nematic orientation defined by OP \mathbf{Q} and does not change the amplitude of the tensor \mathbf{P} . In the isotropic phase $|\mathbf{Q}|$ is practically zero, which makes \mathbf{F}_Q very small compared to the rotational diffusion term in equation (6).

A.2. Reduction to a scalar system

In order to convert our system to a set of scalar equations, we denote:

$$\mathbf{Q} = \begin{pmatrix} n_1 & n_2 \\ n_2 & -n_1 \end{pmatrix}, \quad \mathbf{P} = \begin{pmatrix} p_1 & p_2 \\ p_2 & -p_1 \end{pmatrix}. \quad (\text{A.9})$$

We transform our system into a set of scalar equations for two complex and three scalar variables: $n = n_1 + in_2$, $p = p_1 + ip_2$, c , w , Ψ (equations (2) and (3) can be replaced with a single equation for the stream function Ψ defined as $v_x = \partial_y \Psi$, $v_y = -\partial_x \Psi$). For equations (1), (6) this transformation is performed by summing up (1, 1) component with its (1, 2) component multiplied by the complex unity i . As a result, the nondimensionalized version of equation (1) can be written in the following form (for details see SI to [21]):

$$\begin{aligned} \frac{\partial n}{\partial t} + \Psi_y n_x - n_y \Psi_x - \frac{\Gamma}{\text{Er}} \nabla^2 n - i\xi \left(|n|^2 - \frac{1}{2} \right) \square^2 \Psi \\ + n \left(\frac{\Gamma}{\text{Er}} (a + 2b|n|^2) + i\nabla^2 \Psi \right) + i\xi n^2 \square^{*2} \Psi \\ - in \text{Im}(n^* \mathbf{F}_{\text{ext}}) - in \mathcal{I}(\vec{r}) \text{Im}(n^* \mathbf{F}_{\text{anch}}) = 0. \end{aligned} \quad (\text{A.10})$$

Here the following differential operators are used:

$$\begin{aligned} \square &= \partial_x + i\partial_y, & \square^* &= \partial_x - i\partial_y, \\ \nabla^2 &= \square \cdot \square^* = \partial_x^2 + \partial_y^2, \\ \square^2 &= \partial_x^2 + 2i\partial_x \partial_y - \partial_y^2, \\ \square^{*2} &= \partial_x^2 - 2i\partial_x \partial_y - \partial_y^2. \end{aligned} \quad (\text{A.11})$$

Correspondingly, equations (2) and (3) are reduced to a single equation for the stream function Ψ . This can be performed by applying a curl operation to equation (4):

$$\nabla \times \begin{pmatrix} p_1 \\ p_2 \end{pmatrix} \equiv \partial_x p_2 - \partial_y p_1. \quad (\text{A.12})$$

The nondimensionalized version of equation (2) is:

$$\text{Er}(\nabla^4 \Psi - \zeta \nabla^2 \Psi) = \text{Im}[\square^{*2}(c_s + \text{Er} c_{\text{act}}) + \nabla^2(c_a)], \quad (\text{A.13})$$

where

$$\begin{aligned} c_s &= -(\square n)(\square^* n^*) + \xi(1 - 4|n|^2)(a + 2c|n|^2)n \\ &\quad + \xi(2(\nabla^2 n^*)n^2 + (2|n|^2 - 1)\nabla^2 n), \\ c_a &= 2 \text{Im}(n \nabla^2 n^*), \\ c_{\text{act}} &= \Lambda c p / 2. \end{aligned} \quad (\text{A.14})$$

Here the Ericksen number is $\text{Er} = \eta V_0 l / K$. In equation (4) bacteria orientation unit vector is defined as $\vec{p} = (\cos(\phi), \sin(\phi))$, where $\phi \in [-\pi/2, \pi/2]$ is defined as $\phi = \text{Arctan}(p_2, p_1)/2$. equation (4) is already in scalar form. Equation (6) is reduced to a scalar equation for the complex variable $p = p_1 + ip_2$ in a similar way as equation (1). As a result, we get:

$$\frac{\partial p}{\partial t} = a_p p - 4c_p |p|^2 p + \frac{4}{\tau_0} i p \text{Im}(n p^*) + D_r \nabla^2 p. \quad (\text{A.15})$$

A.3. Calculation of tactoid's topological charge

In order to determine the topological charge of a particular region (for example, the region that encloses the tactoid), the sum of phase differences was calculated along the contour enclosing this region in the counterclockwise direction. Let us denote the nematic angle of those points in counterclockwise order as θ_i , $i = 1, \dots, N$. The topological charge of the region enclosed by the contour is:

Table A1. Model parameters.

Parameter	Value	Description
Parameters of LC		
K	10–15	Elastic constant (pN)
Er	3.75	Ericksen number
Γ	1	Relaxation rate (m s kg^{-1})
η	0.5	Isotropic viscosity ($\text{kg m}^{-1} \text{s}^{-1}$)
ξ_{exter}	0–0.6	Wall anchoring strength (s^{-1})
ξ_{anch}	2000–2500	I–N anchoring strength ($\mu\text{m}^2 \text{s}^{-1}$)
h	20–30	Thickness (μm)
ξ	0.9	Aspect ratio parameter
a	–2–0.4	Landau–de Gennes coefficient (N m^{-2})
c	0.8	Landau–de Gennes coefficient (N m^{-2})
a_p	0.4	LdG coefficient in P equation (N m^{-2})
c_p	0.8	LdG coefficient in P equation (N m^{-2})
Parameters for bacterial transport		
l	5	Bacterial length (μm)
V_0	15	Bacterial speed ($\mu\text{m s}^{-1}$)
τ	50–100	Reversal time (s)
τ_p	1	Bacteria relaxation time (s)
D_c	200–300	Concentration diffusion ($\mu\text{m}^2 \text{s}^{-1}$)
D_r	100–200	Rotational diffusion ($\mu\text{m}^2 \text{s}^{-1}$)
Λ	187.5	Dipolar strength (pN μm)

$$s = \frac{1}{4\pi} \left[\sum_{k=1}^{k=N} \text{mod}(2(\theta_{\text{mod}(k+1,4)} - \theta_k) + \pi, 2\pi) - N\pi \right]. \quad (\text{A.16})$$

For isotropic tactoid, the rectangular contour was used (see the red rectangle in figure 1(a)). For the nematic tactoid, the circular region was used with radius $R = 0.99R_0$, where R_0 is the tactoid's radius (see figure 3(a)).

A.4. Scaling of model parameters

All the lengths are normalized by the bacterial length $l = 5 \mu\text{m}$. Velocities are normalized by the bacterial velocity $V_0 = 15 \mu\text{m s}^{-1}$. Time is normalized by l/V_0 . Concentrations are normalized by l^{-3} . Viscosities are normalized by $\eta = 0.5 \text{ kg m}^{-1} \text{s}^{-1}$. The Landau–de Gennes coefficients a and c are normalized by K/l^2 , where $K = 10 \text{ pN}$ is the average elasticity constant. Correspondingly, the diffusion coefficient D_c is normalized by lV_0 , viscous friction coefficient ζ by η/l^2 , the dipole strength Λ by $\eta l^2 V_0$, Γ by $1/\eta$, wall anchoring strength ξ_{exter} normalized by V_0/l , I–N anchoring strength ξ_{anch} by $V_0 l$. The Ericksen number is $Er = \eta l V_0 / K = 3.75$. The parameters used in our model are listed in table A1.

Appendix B. Additional integration results

The results for the isotropic tactoid in nematic medium with homeotropic I–N anchoring are shown in figure B1. Here we placed the tactoid along the y -axis. The dependencies of the tactoid topological charge and relative concentration difference on the wall anchoring, bacteria concentration and the size of the tactoid are shown in figures B1(C)–(F). The charge magnitude grows with the bacterial concentration and tactoid's size in agreement with the Fokker–Plank model. However, the charge magnitude decreases with the wall anchoring strength ξ_{exter} . This can be explained by the aligning effect of the wall anchoring: topological defects predominantly move in the direction normal to the wall anchoring or parallel to the y -axis (see figure B1(B)). As a result, the effective area of the tactoid that is exposed to the topological defects becomes smaller for strong wall anchoring, in contrast to the case with planar anchoring, where we placed the tactoid along the x -axis (see figure 1).

The dependence of the tactoid's topological charge and relative concentration difference for the nematic tactoids in isotropic medium with homeotropic I–N anchoring is shown in figure B2. Topological charge magnitude grows with bacterial concentration and tactoid's size in agreement with the Fokker–Plank model.

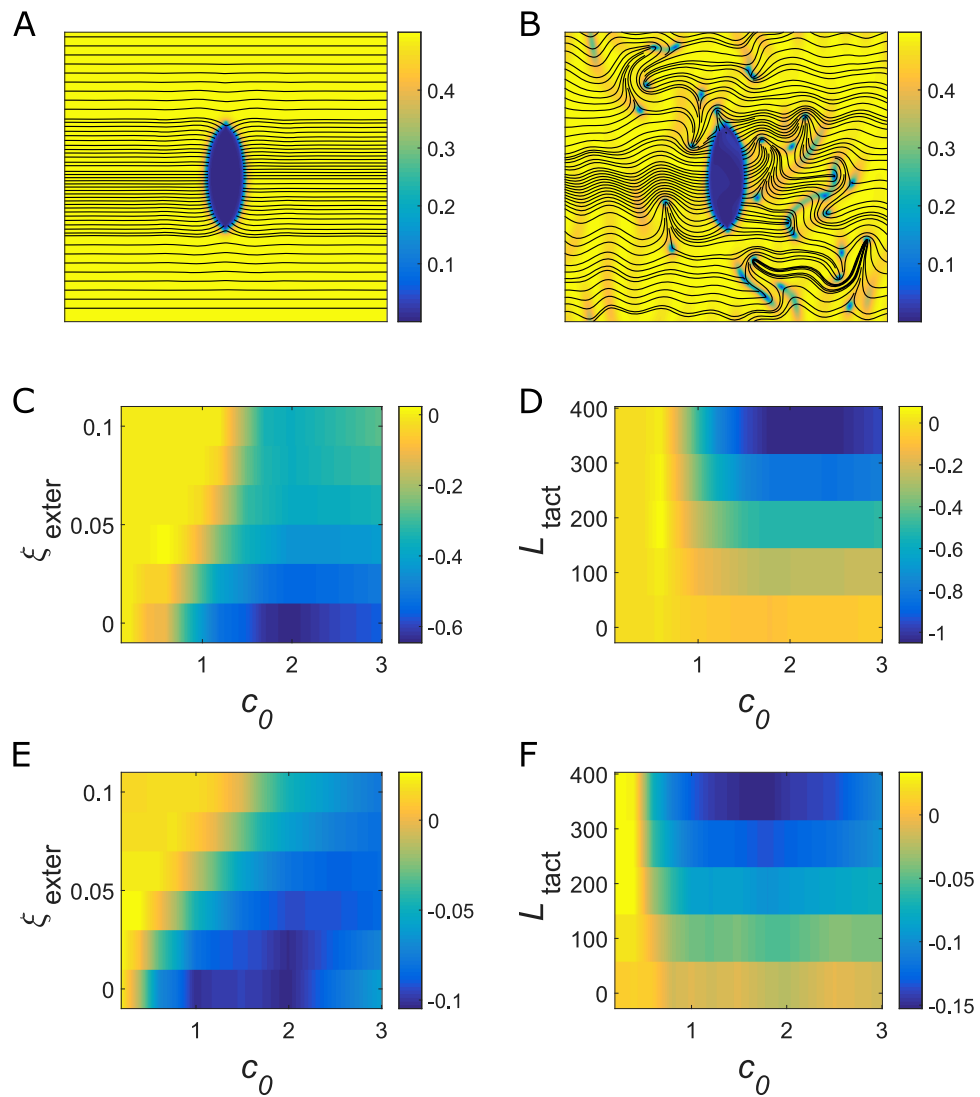


Figure B1. Isotropic tactoid in a nematic medium with homeotropic I–N anchoring. Here we placed the tactoid parallel to the y-axis. Nematic fields for mean bacteria concentration $c_0 = 0.4$ (A) and $c_0 = 0.6$ (B). Tactoid size (the length of the major axis) is $L_{\text{tact}} = 180$, wall anchoring strength is $\xi_{\text{exter}} = 0.02$. The tactoid topological charge $\langle s_t \rangle$ (C) and relative concentration difference $\langle c_t \rangle$ (E) versus wall anchoring strength ξ_{exter} and mean bacteria concentration c_0 . Here the tactoid size is fixed $L_{\text{tact}} = 180$. The tactoid charge $\langle s_t \rangle$ (D) and relative concentration difference $\langle c_t \rangle$ (F) versus tactoid size L_{tact} and mean bacteria concentration c_0 . Here the wall anchoring strength is fixed $\xi_{\text{exter}} = 0.02$.

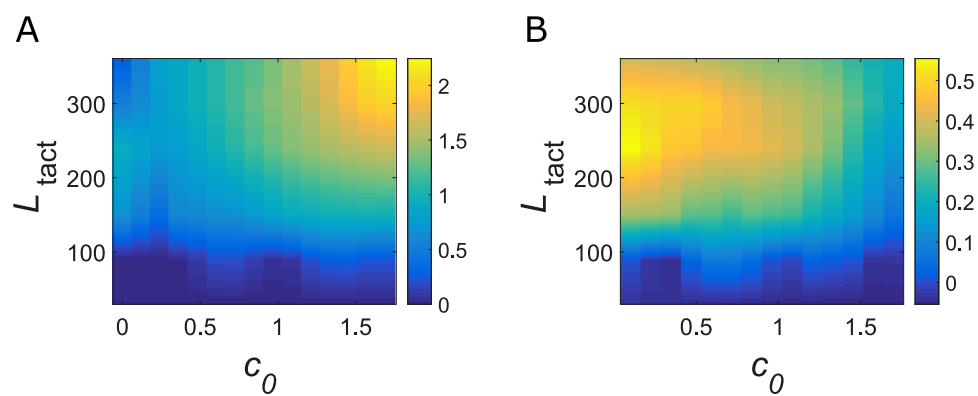
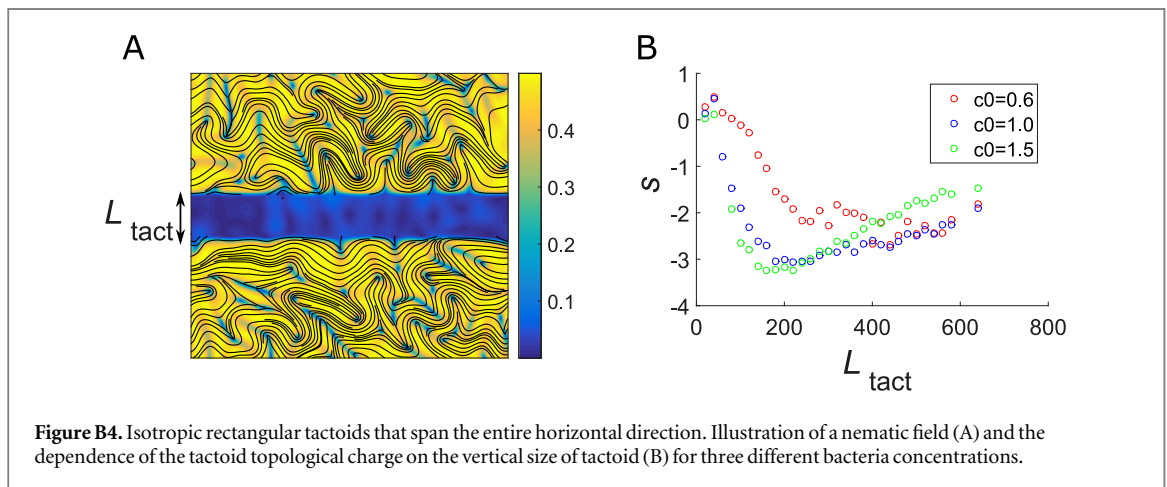
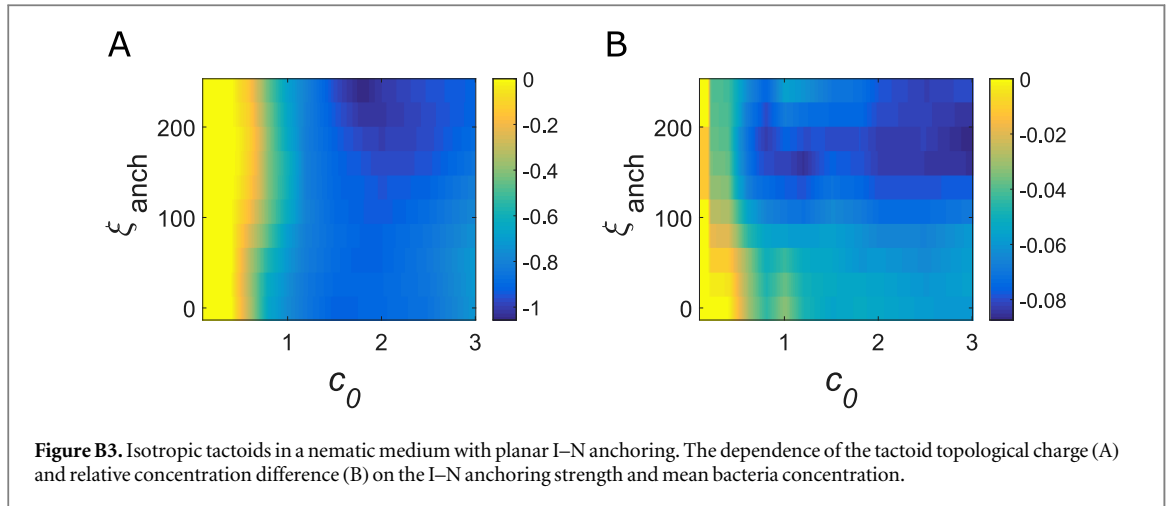


Figure B2. Nematic tactoids in isotropic medium with homeotropic I–N anchoring. The dependence of the tactoid topological charge (A) and relative concentration difference (B) on the tactoid size and mean bacteria concentration.



Relative concentration difference is positive (since the I–N anchoring is homeotropic) with its maximum attained for small bacteria concentrations and large sizes.

Next, we investigated the dependence of the tactoid topological charge and relative concentration difference on the strength of I–N anchoring ξ_{anch} . The relevant dependencies are shown in figure B3 for the isotropic tactoids with planar anchoring. One sees that the tactoid topological charge slightly increases in magnitude with the I–N anchoring strength. Relative concentration difference also depends on the I–N anchoring strength, but the effect is relatively weak too. These dependencies indicate that the energy barrier on the I–N interface arises not exclusively due to the I–N anchoring, but also due to the gradients of the OP's amplitude.

In addition, we tested our prediction against rectangular tactoids that span along the entire horizontal direction (see figure B4(A)). We varied the tactoid width (vertical size), keeping the tactoid surface area constant, and gathered the statistics for three different bacterial concentrations. The dependence of the tactoid topological charge on the tactoid vertical size is shown in figure B4(B). One sees that for sufficiently large tactoid sizes, the topological charge practically does not depend on the tactoid width.

Appendix C. Fokker–Plank model

To support our hypothesis, we developed a stationary 1D Fokker–Plank description. Consider an 1D system $x \in [0, L]$, occupied by nematic phase. We place an isotropic tactoid to the left of the nematic place with a thin I–N interface of the width δ located at $x \in [0, \delta]$ (see figure C1). The system is populated by positive and negative defects that can reside either in the nematic phase or on the I–N interface. The total numbers of positive (N^+) and negative (N^-) defects are the same: $N^+ = N^- = N$. We assume positive defects are more mobile (since $+1/2$ defects move approximately 5 times faster than $-1/2$ defects). We also introduce a potential barrier that prevents defects from escaping the tactoid, which is defined by a step function:

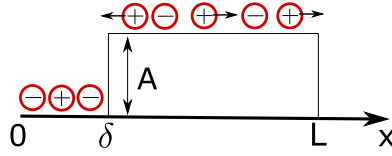


Figure C1. Illustration of the 1D system described by the Fokker–Plank model.

$$F(x) = \begin{cases} 0, & \text{for } 0 < x < \delta, \\ A, & \text{for } x > L, \end{cases} \quad (\text{C.1})$$

where $A > 0$ is the strength of the barrier.

We assume that defects interact similarly to point electrical charges (those with the same topological charge repel, those with different attract) and the interaction strength decays with distance as $1/x$. Thus, the drift consists of two contributions: one due to defect interaction and another due to a barrier on the tactoid's surface. The corresponding Langevine equations for each individual defect can be written in the following form:

$$\begin{aligned} \partial_t x_i^+ &= F'(x_i^+) + \mu \left(\sum_{j=0}^N \frac{1}{x_j^- - x_i^+} - \sum_{j=0, j \neq i}^N \frac{1}{x_j^+ - x_i^+} \right) + \xi^+, \\ \partial_t x_i^- &= F'(x_i^-) + \mu \left(\sum_{j=0}^N \frac{1}{x_j^+ - x_i^-} - \sum_{j=0, j \neq i}^N \frac{1}{x_j^- - x_i^-} \right) + \xi^-, \end{aligned} \quad (\text{C.2})$$

where μ is the interaction strength, ξ^\pm are random forces with the magnitude D^\pm . We introduce the probability density distribution functions of positive and negative defects ($P^+(x, t)$ and $P^-(x, t)$ correspondingly). The sums in equation (C.2) can be written as integrals over P^\pm : $\sum B_i = \int_0^\infty BP(x)dx$. As a result, we obtain a coupled Fokker–Plank equations for the probability density distribution functions of positive and negative defects ($P^+(x, t)$ and $P^-(x, t)$ correspondingly):

$$\begin{aligned} \partial_t P^+(x, t) &= D^+ \partial_{xx} P^+ - \partial_x \left[\left(-F'(x) + \mu \int_0^L \frac{P^+(x', t) - P^-(x', t)}{x - x'} dx' \right) P^+(x, t) \right], \\ \partial_t P^-(x, t) &= D^- \partial_{xx} P^- - \partial_x \left[\left(-F'(x) + \mu \int_0^L \frac{P^-(x', t) - P^+(x', t)}{x - x'} dx' \right) P^-(x, t) \right]. \end{aligned} \quad (\text{C.3})$$

In order to simplify the equations, we assume D^+ is very large, so that positive defects are distributed uniformly: $P^+(x, t) = P_0$. Our goal is to find a stationary probability distribution function for negative defects:

$$\partial_x \left[\left(-F'(x) + \mu \int_0^L \frac{P^-(x') - P_0}{x - x'} dx' \right) P^-(x) \right] = D^- \partial_{xx} P^-(x). \quad (\text{C.4})$$

We integrate equation (C.4) over x to obtain:

$$\left(-F'(x) + \mu \int_0^L \frac{P^-(x') - P_0}{x - x'} dx' \right) P^-(x) = D^- \partial_x P^-(x) + C. \quad (\text{C.5})$$

In order to find the constant C , consider the limit $L \rightarrow \infty$. For $x \rightarrow \infty$, the first three terms in equation (C.5) go to zero: the barrier is constant for $x > \delta$, $P^-(x \gg L_1) = P_0$ (since we always have the same amount of negative and positive defects), so that $\partial_x P^- = 0$. The interaction term is also zero, since at large x' the numerator is zero, and at small x' the denominator is very large. Thus, $C = 0$, and we obtain:

$$\left(-F'(x) + \mu \int_0^L \frac{P^-(x', t) - P_0}{x - x'} dx' \right) P^-(x, t) = D^- \partial_x P^-. \quad (\text{C.6})$$

Let us denote:

$$I_{\text{int}}(x) = \int_0^L \frac{P^-(x', t) - P_0}{x - x'} dx'. \quad (\text{C.7})$$

Then our equation can be written in a compact form:

$$(-F'(x) + \mu I_{\text{int}}(x)) P^-(x) = D^- \partial_x P^-(x). \quad (\text{C.8})$$

This equation can be integrated again:

$$P^-(x) = Ce^{-(F(x)+\mu \int I_{\text{int}}(x)dx)/D^-}. \quad (\text{C.9})$$

Here C is the arbitrary integration constant. We can interchange the integration order and integrate the interaction term $I_{\text{int}}(x)$ over x :

$$\int I_{\text{int}}(x)dx = \int_0^L (P^-(x') - P_0) \ln\left(\frac{|x-x'|}{L}\right) dx'. \quad (\text{C.10})$$

Note that we omit the integration constant, as long as we already have one in equation (C.9). We assume a small interaction strength: $\mu = \epsilon\mu_1$, where $\epsilon \ll 1$. Thus, in equation (C.9) we can write the exponent of a sum as a product of two exponents and expand the second one in Maclaurin series. We also expand the constant $C = C_0 + \epsilon C_1 + \dots$. As a result, we obtain:

$$P^-(x) = (C_0 + \epsilon C_1) e^{-F(x)/D^-} \left(1 - \epsilon \frac{\mu_1}{D^-} \int_0^L (P^-(x') - P_0) \ln\left(\frac{|x-x'|}{L}\right) dx' + O(\epsilon^2) \right). \quad (\text{C.11})$$

We solve equation (C.11) using the asymptotic expansion $P^-(x) = P_0^-(x) + \epsilon P_1^-(x) + \dots$. Substituting this into equation (C.11), we immediately obtain the solution for the zeroth order:

$$P_0^-(x) = C_0 e^{-F(x)/D^-}. \quad (\text{C.12})$$

This solution describes the defect distribution in the system without interaction. Constant C_0 can be found from the normalization condition, if we know the mean defect density P_0 . Using equation (C.1), we get:

$$P_0 = \frac{1}{L} \int_0^L P_0^-(x) dx = \frac{1}{L} (C_0 \delta + C_0 (L - \delta) e^{-A/D^-}), \quad (\text{C.13})$$

so that:

$$C_0 = \frac{P_0 L e^{A/D^-}}{L - \delta + \delta e^{A/D^-}}. \quad (\text{C.14})$$

Thus, in the zeroth order:

$$P_0^-(x) = \frac{P_0 L e^{(A-F(x))/D^-}}{L - \delta + \delta e^{A/D^-}}. \quad (\text{C.15})$$

From equation (C.11) we can obtain $O(\epsilon)$ equations:

$$P_1^-(x) = C_1 e^{-F(x)/D^-} - \frac{\mu_1 P_0^2 L e^{(A-F(x))/D^-}}{D^-(L - \delta + \delta e^{A/D^-})} \int_0^L \left(\frac{L e^{(A-F(x'))/D^-}}{L - \delta + \delta e^{A/D^-}} - 1 \right) \ln\left(\frac{|x-x'|}{L}\right) dx'. \quad (\text{C.16})$$

Let us consider the second term in equation (C.16). We can represent the integral as a sum of two integrals: one from 0 to δ , another from δ to L . Let us denote these two integrals as $r_1(x)$ and $r_2(x)$:

$$r_1(x) \equiv \left(\frac{L e^{A/D^-}}{L - \delta + \delta e^{A/D^-}} - 1 \right) \int_0^\delta \ln\left(\frac{|x-x'|}{L}\right) dx', \quad (\text{C.17})$$

$$r_2(x) \equiv \left(\frac{L}{L - \delta + \delta e^{A/D^-}} - 1 \right) \int_\delta^L \ln\left(\frac{|x-x'|}{L}\right) dx'. \quad (\text{C.18})$$

We can calculate the integrals, and as result, we obtain:

$$r_1(x) = \frac{(e^{A/D^-} - 1)(L - \delta) \left(-\delta + x \log \frac{x}{L} + (\delta - x) \log \frac{|x-\delta|}{L} \right)}{L - \delta + \delta e^{A/D^-}}, \quad (\text{C.19})$$

$$r_2(x) = -\frac{(e^{A/D^-} - 1)\delta}{L - \delta + \delta e^{A/D^-}} \left(-L + \delta + (L - x) \log \frac{L-x}{L} + (x - \delta) \log \frac{|x-\delta|}{L} \right). \quad (\text{C.20})$$

Substituting everything into equation (C.16), we obtain the P^- :

$$P_1^- = C_1 e^{-F(x)/D^-} - \frac{\mu_1 P_0^2 L}{D^-} e^{(A-F(x))/D^-} (e^{A/D^-} - 1) \frac{x(L - \delta) \ln \frac{x}{L} - (L - x)\delta \ln \frac{L-x}{L} - L(x - \delta) \ln \frac{|x-\delta|}{L}}{(L - \delta + \delta e^{A/D^-})^2} \quad (\text{C.21})$$

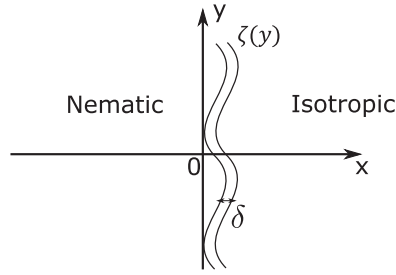


Figure D1. Nematic-isotropic phase coexistence with thin I-N interface.

In order to find C_1 , one has to use the normalization condition for the function P_1^- :

$$\int_0^L P_1^-(x) dx = 0. \quad (\text{C.22})$$

Substituting P_1^- from (C.21) into (C.22), we derive the expression for C_1 :

$$C_1 = \frac{\mu_1 P_0^2 L}{2D^-} e^{A/D^-} (e^{A/D^-} - 1) \frac{\delta^2 (L - \delta - e^{A/D^-} (2L - \delta)) \ln \frac{L-\delta}{\delta} - L^2 (L - \delta - e^{A/D^-} \delta) \ln \frac{L-\delta}{L}}{(L - \delta + \delta e^{A/D^-})^3}. \quad (\text{C.23})$$

Thus, our solution up to the first order of ϵ is $P^- = P_0^- + \epsilon P_1^-$, where P_0^- is given by (C.15) and P_1^- is given by (C.21), (C.23). We can find the mean tactoid charge density using the following formula:

$$s = \frac{1}{\delta} \int_0^\delta (P_0 - P^-(x)) dx. \quad (\text{C.24})$$

Substituting P^- , after some algebra, we obtain:

$$s = -\frac{P_0(L - \delta)(e^{A/D^-} - 1)}{L - \delta + \delta e^{A/D^-}} \times \left(1 - \epsilon \frac{\mu_1 L^2 P_0 e^{A/D^-}}{D} \frac{\delta \log \frac{L-\delta}{\delta} - L \log \frac{L-\delta}{L}}{(L - \delta + e^{A/D^-} \delta)^2} \right). \quad (\text{C.25})$$

Note that for finite tactoid in an infinite medium $L \gg \delta$, the interaction term diverges:

$$s \approx -P_0(e^{A/D^-} - 1) \left(1 - \epsilon \frac{\mu_1 P_0 e^{A/D^-}}{D} \delta \log \frac{L}{\delta} \right). \quad (\text{C.26})$$

Equation (C.26) still holds for large L provided that the interaction strength μ_1 is sufficiently small. It predicts parabolic dependence of the tactoid's charge density on defect density P_0 . In addition, in this model we did not include the tactoid size explicitly (since topological defects can only exist in the nematic medium or on the I-N interface). Therefore, the charge density is independent of the tactoid size.

Appendix D. Relation to Rapini–Papoular approach

It is possible to show that our dynamical treatment of the I-N anchoring is equivalent to the conventional Rapini–Papoular approach, where the additional I-N energy is introduced into the expression for the elastic energy [43]. Meanwhile, we can justify that the normal to the I-N interface is parallel to the gradient of the OP's amplitude $|Q|$ for smooth interfaces.

Ignoring the isotropic tension (as long as a tactoid's area is nearly constant), the anisotropic tension in the Rapini–Papoular approach is of the following form:

$$\sigma = w(\theta - \theta_0)^2, \quad (\text{D.1})$$

where w is the strength of the anisotropic anchoring, θ_0 is an easy angle (the angle between the normal to the interface and the easy direction), and θ is the nematic angle.

Consider a steady-state regime with zero fluid velocity and without the wall anchoring. Under these assumptions, equation (A.10) can be written in the following form:

$$\nabla^2 n + a(x, y)n - cn|n|^2 + \xi_t \mathcal{I}(x, y) \text{in Im}(n^* F_t) = 0. \quad (\text{D.2})$$

Here $a(x, y)$ and c are Landau–de Gennes coefficients, where the coefficient $a(x, y)$ is set according to (7). The factor Er/Γ is absorbed in the anchoring strength, where we defined $\xi_t = \xi_{\text{anch}} \text{Er}/\Gamma$. Consider the quasi 1D problem with a nematic phase in the region $x < 0$ and isotropic phase in the region $x > 0$. Let us denote the interface shape with function $\zeta(y)$ (see figure D1). According to our definition of the coefficient a , for the given interface shape: $a(x, y) = a(x - \zeta(y))$. Equation (D.2) can be written as two scalar equations for amplitude q and phase θ , if we substitute $n = qe^{i\theta}$ and separate the real and the imaginary parts:

$$\nabla^2 q + a(x - \zeta(y))q - bq^3 - q((\partial_x \theta)^2 + (\partial_y \theta)^2) = 0, \quad (\text{D.3})$$

$$q\nabla^2 \theta + 2(q_y \theta_y + q_x \theta_x) + \xi_t q^2 (\nabla q)^2 (\theta_0 - \theta) = 0. \quad (\text{D.4})$$

In the last term of equation (D.4) there is an additional factor $(\nabla q)^2$ that comes from the definition of the easy direction \vec{f} . In addition, we omitted the step function $\mathcal{I}(x, y)$ since here we only consider the I–N interface and replaced $\sin(\theta_0 - \theta)$ with $\theta_0 - \theta$ assuming that this difference is small.

Here we make two main assumptions: (i) thin and smooth I–N interface: $\delta\zeta'(y) \ll \zeta(y)$, where δ is the interface thickness, and (ii) spatial derivatives of the nematic angle are much smaller than those of the OP's amplitude $\nabla q \approx q/\delta \gg \nabla \theta$. Assumption (i) is valid as long as we define tactoids with a smooth interface. Assumption (ii) is valid as long as the deviations of the nematic angle from the easy angle on the I–N interface are small.

Assume that the solution for the unperturbed interface $\zeta(y) = 0$ is known: $q(x) = G(x)$, $\theta(x) = 0$. The solution $G(x)$ is constant in the nematic phase, zero in the isotropic phase and decays quickly in a narrow I–N interface region. Let us now consider a perturbation to the interface shape $\zeta(y)$. With the assumptions (i) and (ii), the solution of equation (D.3) is $n(x, y) = G(x - \zeta(y))$. In this case normal to the interface vector $\nabla(x - \zeta(y)) = (1, -\zeta'(y))$ is parallel to the gradient of OP's amplitude $\nabla G(x - \zeta(y)) = G'(1, -\zeta'(y))$. This justifies that the normal to the interface is directed parallel to the OP's amplitude gradient.

Next, consider equation (D.4) and neglect all the y -derivatives (using assumption (i)):

$$q\theta_{xx} + 2q_x \theta_x + \xi_t q^2 q_x^2 (\theta_0 - \theta) = 0. \quad (\text{D.5})$$

Here we argue that the first term governs the dynamics in nematic phase (elasticity), whether the second and third are the leading terms on the I–N interface since the second term contains q_x that is much greater than any θ derivatives and the third term counterbalances it. Thus, we neglect the first term and integrate equation (D.5) over the width of the I–N interface:

$$\int_0^\delta (2q_x \theta_x + \xi_t q^2 q_x^2 (\theta_0 - \theta)) dx = 2q\theta_{x|0}^\delta - 2 \int_0^\delta q\theta_{xx} dx + \xi_t \frac{q^4}{\delta} (\theta_0 - \theta). \quad (\text{D.6})$$

Here integration by parts has been used. In the third term of the right-hand side, we neglected the numerical factors when integrating $q^2 q_x^2$ and assumed $q_x \approx q/\delta$ under the integral sign. On the right-hand side of this expression, we can neglect the second term, as this integral is proportional to δ (note, that this term would have been generated by the first term in equation (D.5), that we have already neglected). Thus we obtained that on the I–N interface:

$$2q\theta_x + \xi_t \frac{q^4}{\delta} (\theta_0 - \theta) = 0. \quad (\text{D.7})$$

This equation is similar to the boundary conditions that one obtains when minimizing the nematic free energy with Rapini–Papoular contribution (see chapter 5 in [57]):

$$\pm \frac{\partial f_{\text{FO}}}{\partial \theta'} + \frac{df_s}{d\theta} = 0, \quad (\text{D.8})$$

where f_{FO} and f_s are the elastic and I–N surface energy densities correspondingly. Plugging in $f_{\text{FO}} = K(\theta')^2/2$, $f_s = w(\theta - \theta_0)^2/2$, we obtain:

$$K\theta' + w(\phi - \theta) = 0. \quad (\text{D.9})$$

By comparing (D.7) and (D.9) and using $\xi_t = \xi_{\text{anch}} \text{Er}/\Gamma$, we find that:

$$\xi_{\text{anch}} = \frac{2\Gamma}{\text{Er}q^3} \frac{\delta}{L_0}. \quad (\text{D.10})$$

Here $L_0 = K/w$ is the anchoring extrapolation length. Plugging in the parameters from our model and a typical value of the anisotropic tension $w = 10^{-4} \text{ J m}^{-2}$, we estimate $\xi_{\text{anch}} \approx 20\text{--}50$. Note that this is a very rough estimate since we neglected all the numerical factors during the integration of equation (D.5). In this work, we typically used the I–N anchoring strength $\xi_{\text{anch}} = 30$.

ORCID iDs

Mikhail M Genkin  <https://orcid.org/0000-0002-5476-7683>

References

- [1] Ramaswamy S 2010 The mechanics and statistics of active matter *Annu. Rev. Condens. Matter Phys.* **1** 323–45
- [2] Bialek W, Cavagna A, Giardinà I, Mora T, Silvestri E, Viale M and Walczak A M 2012 Statistical mechanics for natural flocks of birds *Proc. Natl Acad. Sci. USA* **109** 4786–91
- [3] Becco C, Vandewalle N, Delcourt J and Poncin P 2006 Experimental evidences of a structural and dynamical transition in fish school *Physica A* **367** 487–93
- [4] Dombrowski C, Cisneros L, Chatkaew S, Goldstein R E and Kessler J O 2004 Self-concentration and large-scale coherence in bacterial dynamics *Phys. Rev. Lett.* **93** 098103
- [5] Sokolov A, Aranson I S, Kessler J O and Goldstein R E 2007 Concentration dependence of the collective dynamics of swimming bacteria *Phys. Rev. Lett.* **98** 158102
- [6] Nedelec F J, Surrey T, Maggs A C and Leibler S 1997 Self-organization of microtubules and motors *Nature* **389** 305–8
- [7] Sanchez T, Chen D T N, DeCamp S J, Heymann M and Dogic Z 2012 Spontaneous motion in hierarchically assembled active matter *Nature* **491** 431
- [8] DeCamp S J, Redner G S, Baskaran A, Hagan M F and Dogic Z 2015 Orientational order of motile defects in active nematics *Nat. Mater.* **14** 1110–5
- [9] Bricard A, Caussin J B, Desreumaux N, Dauchot O and Bartolo D 2013 Emergence of macroscopic directed motion in populations of motile colloids *Nature* **503** 95–8
- [10] Palacci J, Sacanna S, Steinberg A P, Pine D J and Chaikin P M 2013 Living crystals of light-activated colloidal surfers *Science* **339** 936–40
- [11] Sokolov A and Aranson I S 2009 Reduction of viscosity in suspension of swimming bacteria *Phys. Rev. Lett.* **103** 148101
- [12] Lopez H M, Gachelin J, Douarche C, Auradou H and Clement E 2015 Turning bacteria suspensions into superfluids *Phys. Rev. Lett.* **115** 028301
- [13] Sokolov A, Goldstein R E, Feldchtein F I and Aranson I S 2009 Enhanced mixing and spatial instability in concentrated bacterial suspensions *Phys. Rev. E* **80** 031903
- [14] Tuval I, Cisneros L, Dombrowski C, Wolgemuth C W, Kessler J and Goldstein R E 2005 Bacterial swimming and oxygen transport near contact lines *Proc. Natl Acad. Sci. USA* **102** 2277–82
- [15] Sokolov A, Apodaca M M, Grzybowski B A and Aranson I S 2010 Swimming bacteria power microscopic gears *Proc. Natl Acad. Sci. USA* **107** 969–74
- [16] Kaiser A, Peshkov A, Sokolov A, ten Hagen B, Lowen H and Aranson I S 2014 Transport powered by bacterial turbulence *Phys. Rev. Lett.* **112** 158101
- [17] Rusconi R, Guasto J S and Stocker R 2014 Bacterial transport suppressed by fluid shear *Nat. Phys.* **10** 212–7
- [18] Sokolov A and Aranson I S 2016 Rapid expulsion of microswimmers by a vortical flow *Nat. Commun.* **7** 11114
- [19] Zhou S, Sokolov A, Lavrentovich O D and Aranson I S 2014 Living liquid crystals *Proc. Natl Acad. Sci. USA* **111** 1265–70
- [20] Mushenheim P C, Trivedi R R, Tuson H H, Weibel D B and Abbott N L 2014 Dynamic self-assembly of motile bacteria in liquid crystals *Soft Matter* **10** 88–95
- [21] Genkin M M, Sokolov A, Lavrentovich O D and Aranson I S 2017 Topological defects in a living nematic ensnare swimming bacteria *Phys. Rev. X* **7** 011029
- [22] Schaller V, Weber C, Semmrich C, Frey E and Bausch A R 2010 Polar patterns of driven filaments *Nature* **467** 73–7
- [23] Sumino Y, Nagai K H, Shitaka Y, Tanaka D, Yoshikawa K, Chate H and Oiwa K 2012 Large-scale vortex lattice emerging from collectively moving microtubules *Nature* **483** 448–52
- [24] Angelini T E, Hannezo E, Treppe X, Marquez M, Fredberg J J and Weitz D A 2011 Glass-like dynamics of collective cell migration *Proc. Natl Acad. Sci. USA* **108** 4714–9
- [25] Kawaguchi K, Kageyama R and Sano M 2017 Topological defects control collective dynamics in neural progenitor cell cultures *Nature* **545** 327
- [26] Saw T B, Doostmohammadi A, Nier V, Kocgozlu L, Thampi S, Toyama Y, Marcq P, Lim C T, Yeomans J M and Ladoux B 2017 Topological defects in epithelia govern cell death and extrusion *Nature* **544** 212
- [27] Blow M L, Thampi S P and Yeomans J M 2014 Biphasic, lyotropic, active nematics *Phys. Rev. Lett.* **113** 248303
- [28] Doostmohammadi A, Thampi S P and Yeomans J M 2016 Defect-mediated morphologies in growing cell colonies *Phys. Rev. Lett.* **117** 048102
- [29] Tortora L, Park H S, Kang S W, Savaryn V, Hong S H, Kaznatcheev K, Finotello D, Sprunt S, Kumar S and Lavrentovich O D 2010 Self-assembly, condensation, and order in aqueous lyotropic chromonic liquid crystals crowded with additives *Soft Matter* **6** 4157–67
- [30] Mushenheim P C, Trivedi R R, Weibel D B and Abbott N L 2014 Using liquid crystals to reveal how mechanical anisotropy changes interfacial behaviors of motile bacteria *Biophys. J.* **107** 255–65
- [31] Kibble T W B 1976 Topology of cosmic domains and strings *J. Phys. A: Math. Gen.* **9** 1387–98
- [32] Zurek W H 1996 Cosmological experiments in condensed matter systems *Phys. Rep.* **276** 177–221
- [33] Aranson I S, Kopnin N B and Vinokur V M 1999 Nucleation of vortices by rapid thermal quench *Phys. Rev. Lett.* **83** 2600–3
- [34] Eltsov V B, Krusius M and Volovik G E 2005 Vortex formation and dynamics in superfluid ^3He and analogies in quantum field theory *Prog. Low Temp. Phys.* **15** 1–137
- [35] Das A, Sabbatini J and Zurek W H 2012 Winding up superfluid in a torus via Bose–Einstein condensation *Sci. Rep.* **2** 352
- [36] Kim Y K, Shiyankovskii S V and Lavrentovich O D 2013 Morphogenesis of defects and tactoids during isotropic–nematic phase transition in self-assembled lyotropic chromonic liquid crystals *J. Phys.: Condens. Matter* **25** 404202
- [37] Oakes P W, Viamontes J and Tang J X 2007 Growth of tactoidal droplets during the first-order isotropic to nematic phase transition of f-actin *Phys. Rev. E* **75** 061902
- [38] Kaznatcheev A V, Bogdanov M M and Taraskin S A 2002 The nature of prolate shape of tactoids in lyotropic inorganic liquid crystals *J. Exp. Theor. Phys.* **95** 57–63
- [39] Prinsen P and van der Schoot P 2003 Shape and director-field transformation of tactoids *Phys. Rev. E* **68** 021701
- [40] van Bijnen R M W, Otten R H J and van der Schoot P 2012 Texture and shape of two-dimensional domains of nematic liquid crystals *Phys. Rev. E* **86** 051803

- [41] Smith C J and Denniston C 2007 Elastic response of a nematic liquid crystal to an immersed nanowire *J. Appl. Phys.* **101** 014305
- [42] Brochard F and Gennes P G D 1970 Theory of magnetic suspensions in liquid crystals *J. Physique* **31** 691
- [43] Rapini A and Papoular M 1969 Distorsion d'une lamelle nématique sous champ magnétique conditions d'ancrage aux parois *Le J. Phys. Colloq.* **30** C4-54–56
- [44] Saintillan D and Shelley M J 2008 Instabilities, pattern formation, and mixing in active suspensions *Phys. Fluids* **20** 123304
- [45] Giomi L, Bowick M J, Ma X and Marchetti M C 2013 Defect annihilation and proliferation in active nematics *Phys. Rev. Lett.* **110** 228101
- [46] Pismen L M 2013 Dynamics of defects in an active nematic layer *Phys. Rev. E* **88** 050502
- [47] Chandrasekhar S and Ranganath G S 1986 The structure and energetics of defects in liquid-crystals *Adv. Phys.* **35** 507–96
- [48] Pismen L M 1999 *Vortices in Nonlinear Fields: From Liquid Crystals to Superfluids, From Non-Equilibrium Patterns to Cosmic Strings* (Oxford: Oxford University Press)
- [49] Hiemstra T, Vanriemsdijk W H and Bolt G H 1989 Multisite proton adsorption modeling at the solid-solution interface of (hydr)oxides —a new approach: I. Model description and evaluation of intrinsic reaction constants *J. Colloid Interface Sci.* **133** 91–104
- [50] Behrens S H and Grier D G 2001 The charge of glass and silica surfaces *J. Chem. Phys.* **115** 6716–21
- [51] Blatter G, Feigelman M V, Geshkenbein V B, Larkin A I and Vinokur V M 1994 Vortices in high-temperature superconductors *Rev. Mod. Phys.* **66** 1125–388
- [52] McConney M E, Martinez A, Tondiglia V P, Lee K M, Langley D, Smalyukh I I and White T J 2013 Topography from topology: photoinduced surface features generated in liquid crystal polymer networks *Adv. Mater.* **25** 5880–5
- [53] Guo Y B, Jiang M, Peng C H, Sun K, Yaroshchuk O, Lavrentovich O and Wei Q H 2016 High-resolution and high-throughput plasmonic photopatterning of complex molecular orientations in liquid crystals *Adv. Mater.* **28** 2353–8
- [54] Murray B S, Pelcovits R A and Rosenblatt C 2014 Creating arbitrary arrays of two-dimensional topological defects *Phys Rev E* **90** 052501
- [55] Metselaar L, Dozov I, Antonova K, Belamie E, Davidson P, Yeomans J M and Doostmohammadi A 2017 Electric-field-induced shape transition of nematic tactoids *Phys. Rev. E* **96** 022706
- [56] Lintuvuori J S, Wurger A and Stratford K 2017 Hydrodynamics defines the stable swimming direction of spherical squirmers in a nematic liquid crystal *Phys. Rev. Lett.* **119** 068001
- [57] Kleman M and Lavrentovich O D 2003 *Soft Matter Physics: An Introduction* (Berlin: Springer) (<https://doi.org/10.1007/b97416>)